Mineral pressure gauge based on lattice stability and plasmonic enhancement of cobalt titanate under high pressure

Wenming Qi, Pengwei Li, Min Gao [*], Anwar Hushur,[†] and Hongyan Zhang[‡]

Xinjiang Key Laboratory of Solid State Physics and Devices and School of Physics Science and Technology, Xinjiang University, 830017 People's Republic of China

Titanium cobalt oxide CoTiO$_3$ (CTO) with ilmenite structure has attracted considerable attention in functional materials owing to their multiferroic and chemical stability characteristics similar to FeTiO$_3$ and perovskites. However, information about structural stability and lattice deformation of CTO under high pressure remains unclear. Here, we present a unique pressure gauge through a quantitative investigation on the vibrational properties of compressed CTO by *in situ* high-pressure Raman experiments up to 40 GPa. Neither phase transitions nor amorphization has been observed in such pressure range, demonstrating good lattice stability of CTO. These results have been validated by both the Jahn-Teller effect and Fermi resonance. More importantly, we have attempted to elucidate the evolution of Raman signals for a pressure gauge based on the synergistic effect of plasmon-resonance field enhancement. Our findings not only provide direct experimental evidence that CTO stays phase stable up to 40 GPa, but also offer insight to understanding the high-pressure Raman behaviors for other ilmenite based functional materials.

I. INTRODUCTION

Investigating structural stability of multiferroic materials under multiphysics conditions, such as pressure and temperature, has prompted intense interest in temperature- and pressure-induced surface-enhanced Raman spectroscopy (TISERS and PISERS) [1–8]. Additionally, multiferroic ilmenite mineral exhibiting electromagnetic coupling characteristics not only costs less, but also generates electromagnetic enhancement with light excitation under high pressure [9–11]. As a typical rhombohedron multiferroic material, ilmenite cobalt titanate [CoTiO$_3$ (CTO)] has been extensively studied under room conditions due to its multiferroic and chemical stability, including pigments for cloth, glass, and cosmetics as well as gas sensing at the nanoscale [12–14]. However, the structural stability of CTO under high pressure remains unclear, which limits its applications in the fields of ferroelectrics, semiconductors, and sensors [15,16].

Fortunately, high-pressure experiments open opportunities to understand the structural characteristics of matter, especially for ilmenite-structured oxides in Earth's upper mantle and the lunar mantle [17–23]. Understanding electromagnetic interactions between laser and matter under high pressure calls for efficient *in situ* characterization methods. Notably, *in situ* Raman spectroscopy is capable of investigating the changes of molecular structure that matter undergoes under external pressure. Quantitatively investigating the vibration properties of compressed matter by Raman spectroscopy can effectively uncover the information about the structural stability and the lattice deformation [24]. It is widely known that the ruby based on the pressure dependence of the R_1 fluorescence line has been considered as the best pressure gauge until now [25]. However, the frequency of the R_1 line is around 4500 cm^{-1} whereas the Raman peak of most materials is in the range between 100 and 1500 cm^{-1}. In the *in situ* high-pressure Raman experiments, adjusting the spectrometer repeatedly in a wide frequency range will cause a lot of wear and tear to the instrument if we use the ruby pressure gauge. In addition, most researchers add another specialized expensive spectrometer to monitor the pressure in the 4000–5000 cm^{-1} range, which is currently the main solution. Those situations not only hinder the development of high-pressure science in condensed matter physics to a certain degree, but also deviate from the concept of energy saving and emission reduction. Additionally, numerous calibration methods of Raman spectroscopy have also been proposed based on quartz, calcite, dolomite, magnesite, and other minerals [26–29]. Over the past decades, surface plasmon resonance (SPR) has been extensively applied to SERS under room conditions owing to its excellent light confinement and ultrahigh field enhancement. Recently, the emerging subject of nanoplasmonics has appeared regarding the high-pressure environment, especially combining nonmetallic nanostructures such as metal-oxide semiconductors [30–36]. Amid the immensity of these research endeavors, using ilmenite as a pressure gauge based on SPR enhancement has yet to be realized.

In this work, we experimentally investigate the lattice stability of CTO by *in situ* high-pressure Raman spectroscopy up to 40 GPa. A unique pressure gauge has been presented based on the good lattice stability of CTO. More importantly, we desire to elucidate the four-stage evolution of Raman

[*]mgao@xju.edu.cn
[†]anwar.hushur@outlook.com
[‡]zhanghyxj@163.com

signals for a pressure gauge based on the synergistic effect from the Jahn-Teller effect, Fermi resonance, and plasmon-resonance field enhancement. This work allows for further exploration of light-pressure interactions and opens opportunities for wide applications in plasmonic pressure gauges without metal nanoparticles.

II. METHODOLOGY

A. Sample preparation

Cobalt nitrate $[Co(NO_3)_2 \cdot 6H_2O]$, tetra-butyl orthotitanate $(C_{16}H_{36}O_4Ti, TBOT)$, ethanol (C_2H_5O, EA), and citric acid $(C_6H_8O_7, CA)$ were purchased from the Xilong Scientific chemical company and used without further purification. Ilmenite $CoTiO_3$ nanoparticles were synthesized using the sol-gel method [14,16]. First, stoichiometric amounts of cobalt nitrate precursor were dissolved in EA by magnetic stirring for 40 min. Then CA and TBOT were added to the mixed solution to form 1 mol/l transparent solution. The solution was stirred for 6 h, allowed to stand at room temperature for 36 h, and dried in an air dry oven at 90 °C. Finally, ilmenite $CoTiO_3$ nanoparticles were obtained by heating the samples in a sintering muffle furnace at 800 ° for 4 h with a heating rate of 10 °/min in air.

B. Experimental details

In situ high-pressure Raman scattering experiments were carried out with the Horiba iHR550 confocal laser Raman spectrometer. A Cobolt 08-200 mW single frequency diode pumped laser with a 532 nm green line, produced by a single longitudinal mode laser, was used for excitation. The laser spot focused by a Mitutoyo 50× objective lens on the sample was ∼ 2 μm in diameter. The laser power at the sample surface was 15 mW. The laser polarization was 100:1 and the operating temperature was 300 K. The materials inside the diamond anvil cell (DAC) required for high-pressure experiments (anvils, ruby spheres, rhenium gasket, methanol, and ethanol) were purchased from the BJSCISTAR company in China. Type Ia ultralow fluorescence diamond anvils (lower absorption in the visible range) with a 250 μm culet were used in a high-pressure experiment. The samples were loaded in a 120 μm diameter hole in a preindented rhenium gasket of 45 μm thickness. Methanol:ethanol:water = 16 : 3 : 1 was used as a pressure transmitting medium (PTM). Pressure was loaded slowly and monitored closely by the ruby sphere fluorescence method with a precision of 0.1 GPa. Pressure calibration for most DAC experiments is mainly based on the pressure dependence of the R_1 ruby fluorescence line, which is one of the best tools so far for ultrahigh-pressure studies [37]. Before collecting the *in situ* high-pressure spectra, the Raman spectrometer was calibrated by the standard Raman peak of a silicon wafer at 520.7 cm^{-1}.

C. Computational details

Far- and near-field optical scattering properties of different spatial arrangement CTO nano-ovals (CTO NOVs) were simulated using commercial software (COMSOL MULTIPHYSICS) based on finite element methods. The CTO was placed in a homogeneous medium of the PTM. The refractive index of CTO was taken from the experimental data by Martínez-Reina and Amado-González [38]. The dielectric function of CTO was taken from the first-principles calculations based on density functional theory (DFT). The vertical and parallel longitudinal axis of CTO NOVs were set as 60 and 20 nm, respectively. Incident plane waves were excited by the background condition and propagated along the z direction with electric-field polarization along the x direction. The perfectly-matched layer (PML) boundary condition is established in the z-direction. For simulation models, extremely fine physics-controlled meshes were chosen in the whole domain to ensure the convergence and the accuracy of the computation.

III. RESULTS AND DISCUSSION

The green superfine powder CTO sample [Fig. 1(a)] was prepared at the 800 °C 4 h by the sol-gel method. The scanning electron microscope (SEM) image clearly shows that these particles exhibit slight aggregation at the nanoscale [Fig. 1(b)]. Based on the SEM image, 100 nanoparticles were selected in the image randomly. Their particle sizes were counted in the inset of Fig. 1(b) and the results were fitted by a Gaussian function (blue curve), demonstrating that the average particle size of the sample was 64.2 ± 2.2 nm. From the high-resolution transmission electron microscope (HRTEM) image of the sample, we can observe that the particle size is about 60 nm and the profile of the particle is NOVs [Fig. 1(c)]. According to the selective area electron diffraction (SAED) pattern, a polycrystal structure can be obtained [Fig. 1(f)].

The group-theoretical analysis for the trigonal CTO ($R\bar{3}$ space group) predicts 20 phonons and the irreducibility can be written as

$$\Gamma_{total} = 5A_g + 5E_g + 5A_u + 5E_u. \quad (1)$$

CTO exhibits ten Raman active ($\Gamma_{Raman} = 5A_g + 5E_g$), eight infrared active ($\Gamma_{IR} = 4A_u + 4E_u$), and two acoustics ($\Gamma_{acoustic} = A_u + E_u$). A and E denote nondegenerate and doubly degenerate modes, respectively. The Lorentzian fitted profiles for Raman data at ambient conditions are displayed in Fig. 1(d). We can observe that all ten Raman-active modes locate at wave numbers of 162.1, 208, 236.7, 266.9, 335.2, 382, 452.6, 476.2, 601.6, and 699.4 cm^{-1}, respectively, consistent with previous research [39].

Figure 1(e) shows the x-ray diffraction (XRD) Rietveld refinement result at room temperature and room pressure. Space group $R\bar{3}$ (c_{3i}^2, No. 148) and lattice parameters (JCPDS Card no. 77–1373) of $a = b = 5.6385(8)$ Å and $c = 15.879(4)$ Å are obtained at ambient conditions via MDI JADE 6.5 software. A typical XRD pattern of CTO is also used to estimate the average crystallite size "D" of the samples by using the Debye-Scherrer formula as follows:

$$D = K\lambda/(\beta \cos\theta), \quad (2)$$

where D represents the grain size; K, the Scherrer's constant (0.89); λ, the wavelength of the x-ray Cu $K\alpha$ source (1.5406 Å); β, the full width at half maximum (FWHM) of the diffraction peaks; and θ, the diffraction angle. The grain
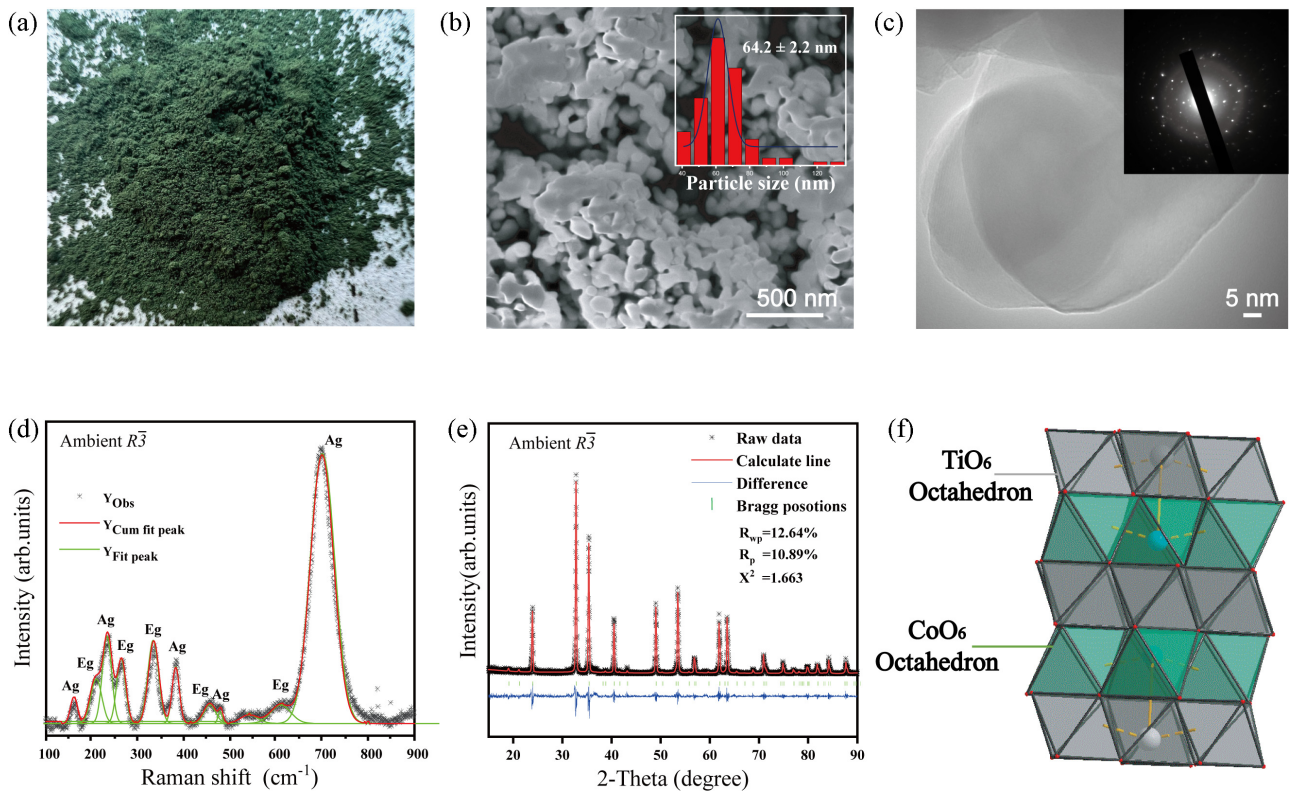
FIG. 1. (a) Optical photograph of $CoTiO_3$ nanopowders. (b) SEM micrograph of $CoTiO_3$ nanopowders. The inset shows the corresponding particle size. (c) A bright-field TEM image of the $CoTiO_3$ sample. The inset shows the corresponding electron diffraction pattern and is obtained from the spot indicated by the open circle. (d) Lorentzian fitted for the Raman spectrum of $CoTiO_3$ at ambient conditions. Symmetry attribution according to Ref. [39]. (e) Rietveld refinement for the pattern of $CoTiO_3$ at ambient conditions. (f) A fragment model of $CoTiO_3$.

size of the sample is calculated to be 55 nm which is consistent with the results of statistics in Fig. 1(b). Ilmenite is the deformation of perovskite with a similar structure. As shown in Fig. 1(f), CTO is built by the face-sharing TiO_6 and CoO_6 units and in accordance with the 1:1 stacking along the c axis. Co and Ti atoms are both in the central octahedral sites and connected by the edge-sharing O atoms between the same layers. The above details of the sample provide the basis information for the high-pressure study.

As shown in Fig. 2(a), the structural stability of the CTO can be directly observed by *in situ* high-pressure Raman spectroscopy. Although a pressure-induced increase in symmetry from the prototype trigonal $R\bar{3}$ symmetry is likely observed, the Raman modes below $500\,cm^{-1}$ become inconspicuous under high pressure. Furthermore, the Eg mode near $600\,cm^{-1}$ disappeared at 19 GPa [Fig. 2(b)], whereas when the pressure is continuously loaded to 40 GPa, most of the Raman modes do not exhibit peculiar changes, such as disappearance, splitting, and the appearance of new peaks. These Raman data suggest that up to 40 GPa CTO does not undergo a phase transition, only a distortion of the TiO_6 octahedron, manifesting the high physical stability since the materials usually exhibit two or three phase transitions within the pressure range of 20 GPa. This result proves the high physical stability of CTO. Notably, the phase stability field of CTO is wider than other known ilmenite-structured compounds under high pressure as

summarized in Fig. 3. This also indicates the existence of a strong kinetic barrier in CTO high-pressure phases. According to the survey that the phase stability field of CTO is wider than other known ilmenite-structured compounds under high pressure, the investigations and its conditions are summarized in Fig. 3. Among them, ilmenite $FeTiO_3$ is stable up to the pressure of 32.2 GPa [40]. The ilmenite $ZnTiO_3$ and ilmenite $MnTiO_3$ are stable within 38.5 and 26.6 GPa, respectively [18,22].

In order to clearly observe the trends of weak peaks between 450 and $650\,cm^{-1}$, the frequency range $150–650\,cm^{-1}$ has been enlarged by a factor of 4 [Fig. 2(b)]. Two conspicuous changes of the Raman spectra in the low-frequency range (P_1: 162.1 and P_3: $236.7\,cm^{-1}$) can be seen up to 40 GPa. Under compression, an energy transfer between a predominant Co-O and a soft Ti-O associated vibration is observed within 40 GPa, and the maximum resonance occurs near 19 GPa. This is considered to be a Fermi resonance phenomenon that was also found in a high-pressure experiment of similar structured ilmenite $FeTiO_3$ [40]. The Raman shift of the two vibration modes between 400 and $500\,cm^{-1}$ changes with the same slope, while the FWHM changes little. This result indicates that the bond length decreases with pressure, whereas the vibration damping has little effect on pressure. Moreover, the disappearance of the Raman mode of the Ti-O bond ($600\,cm^{-1}$) at 19 GPa indicates that the TiO_6 octahedral deformation can be attributed to the pressure-induced Jahn-Teller effect [41]. Similar phenomena also can be found in ABO_3
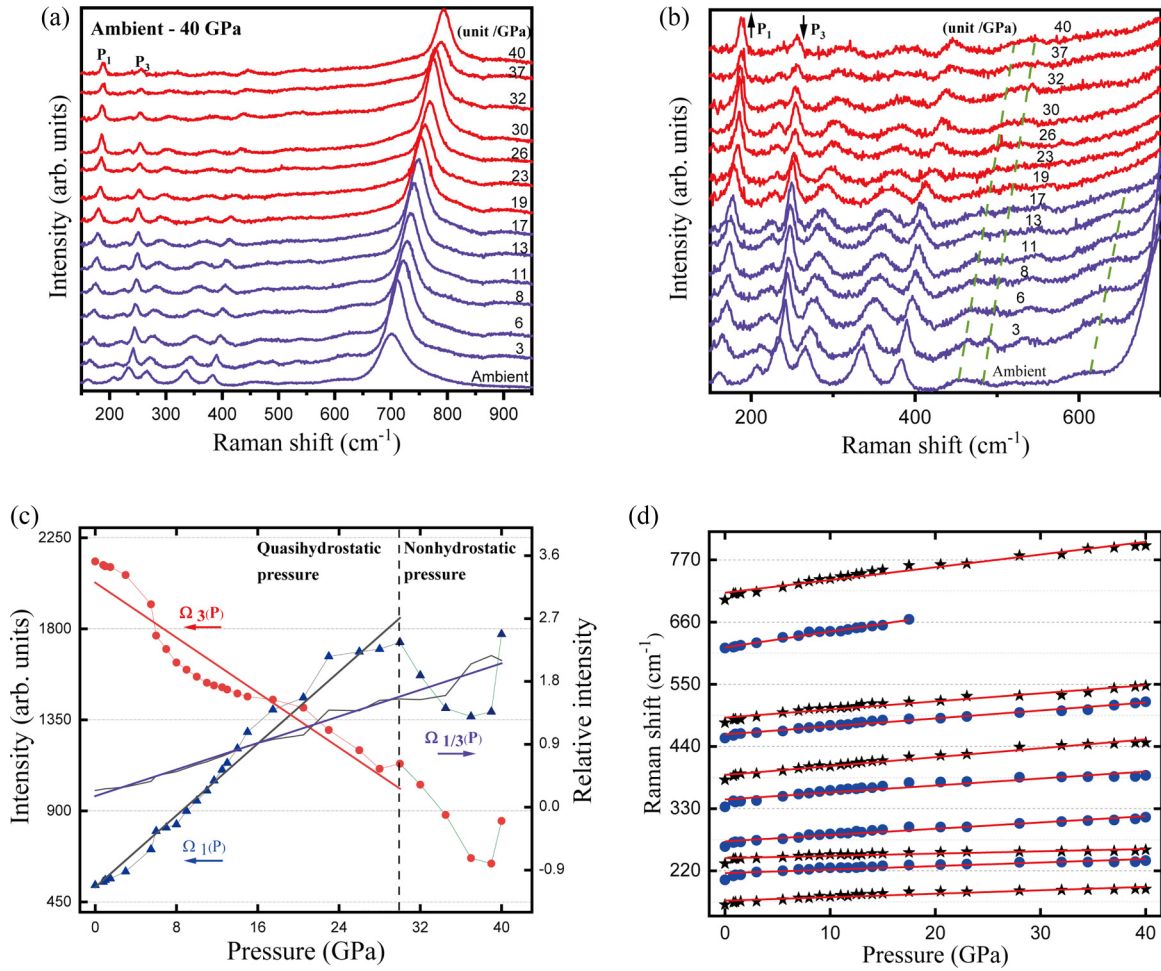
FIG. 2. (a) Raman spectra of $CoTiO_3$ at different pressures in the frequency range of 100–1000 cm^{-1}. (b) The frequency range of 150–650 cm^{-1}. The green dotted lines are a guide to the eye. (c) Pressure dependence of the peak intensity of P_1, P_3, and P_1/P_3, respectively. The straight blue, red, and purple lines represent the intensities of P_1, P_3, and P_1/P_3 after being fitted under pressure, respectively. (d) Pressure dependence of the Raman shift of $CoTiO_3$ phonons up to 40 GPa. Solid circle and solid star symbols represent the Eg and Ag Raman modes, respectively.

family perovskite, because the deformation can resist the increase of lattice energy caused by high pressure [24,41,42], following the principle of lowest energy to make the phase stable at high pressure.
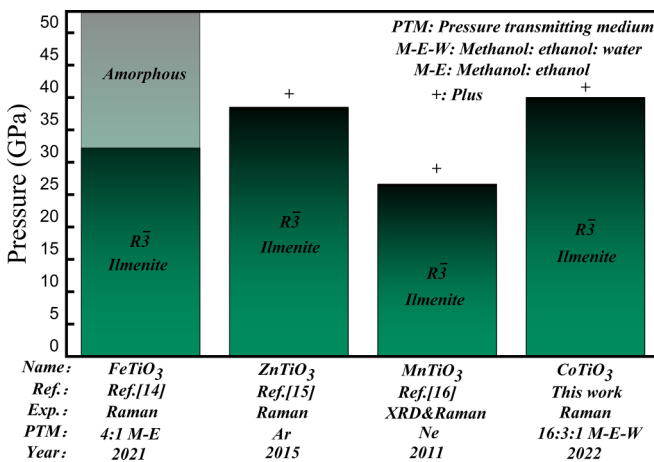
FIG. 3. The research on ilmenite compounds under high pressure.

As shown in Fig. 2(c), the vertical dotted line denotes the boundary between quasihydrostatic and nonhydrostatic pressure effects in the sample since the intensity of two peaks exhibits an irregular change above 30 GPa. The curves of the two peaks' intensity within 30 GPa are linear whereas the linear pressure dependence of P_1/P_3 can last up to 40 GPa. The linear fitted functions are as follows:

$$\Omega_1(P) = 522.89(20.4) + 44.36(1.3)P(0 < P < 30\,\text{GPa}),$$
(3)

$$\Omega_3(P) = 2028.35(34.5) + 33.95(2.2)P(0 < P < 30\,\text{GPa}),$$
(4)

and

$$\Omega_{\frac{1}{3}}(P) = 0.16(0.02) + 0.05(0.001)P(0 < P < 40\,\text{GPa}).$$
(5)

The parts of the nonlinear intensity of P_1 and P_3 in Fig. 2(c) are used to explain the generation of nonhydrostatic pressures in the DAC sample chamber. Although the system is under

TABLE I. The Raman frequencies at 0 GPa (v_{i0}), first pressure derivatives ($\mathrm{d}v/\mathrm{d}p$) of each Raman mode, and mode Grüneisen parameters (γ).

Symmetry	v_{i0} (cm^{-1})	Standard error	$\mathrm{d}v/\mathrm{d}p$ (cm GPa^{-1})	Standard error	γ	Phase
Ag	162.1	1.04	0.61	0.05	0.66	Trigonal
Eg	208	1.25	0.63	0.06	0.53	
Ag	236.7	0.89	0.4	0.04	0.30	
Eg	266.9	1.08	1.14	0.05	0.75	
Eg	335.2	1.73	1.24	0.09	0.65	
Ag	382	1.03	1.58	0.05	0.73	($R\bar{3}$)
Eg	452.6	0.86	1.41	0.04	0.55	
Ag	476.2	1.27	1.43	0.06	0.52	
Eg	601.6	0.89	2.79	0.09	0.82	
Ag	699.4	1.66	2.25	0.08	0.57	

nonhydrostatic pressure between 30 and 40 GPa, the changes of P_1 and P_3 are all synchronized. Therefore, the changes of P_1/P_3 are also linear.

Figure 2(d) shows the pressure dependence of Raman shifts as a function of pressure. All modes show linear trends of blueshifts, suggesting that the chemical bonds generally become shorter with increasing pressure. The slopes of pressure dependences in high-frequency modes are larger than those of low-frequency modes, indicating that the high-frequency modes are more sensitive to pressure than the low-frequency modes. The compressibility of each Raman mode under pressure can be expressed by $\mathrm{d}v/\mathrm{d}p$ and γ, respectively. The functions can be expressed as

$$v_{i0} = v_0 + (\mathrm{d}v/\mathrm{d}p), \qquad (6)$$

and

$$\gamma = (B_0/v_0)(\mathrm{d}v/\mathrm{d}p), \qquad (7)$$

where the v_0 denotes the vibrational frequency at ambient conditions; v_{i0}, the vibrational frequency under 0 GPa; p, the *in situ* pressure; and B_0, the bulk modulus (176 GPa) [43]. The first pressure derivatives and Grüneisen parameter were represented by ($\mathrm{d}v/\mathrm{d}p$) and γ, respectively. The values of v_0, ($\mathrm{d}v/\mathrm{d}p$), and γ for each Raman modes in the trigonal $R\bar{3}$ phase of CTO are summarized in Table I.

As shown in Table I, the minimum value of γ corresponding to the Ag mode near 236.7 cm^{-1} is 0.3, and the maximum value of γ corresponding to the Eg mode near 601.6 cm^{-1} is 0.82. These results indicate that the displacement of cations to each other is less sensitive to pressure than the rotational vibration of anions. Our results also confirmed the DFT calculations by Dubrovin *et al.* that the pressure has a greater effect on the crystal lattice in the *ab* plane (rotational vibration) [39]. In addition, all modes can be fitted linearly, thus indicating that there is no phase transition or amorphization up to 40 GPa.

Furthermore, the pressure-induced Fermi resonance plays an important role in the study of molecules under high pressure [40]. We continue to explore the mechanism of pressure-induced Fermi resonance that governs CTO (see Fig. S1 in the Supplemental Material [44]). Assuming the energies of the Raman modes (P_1 and P_3) as $2hv$ and hv', respectively, the high pressure generated by DAC transfers the

hv energy from P_3 to P_1 vibration mode. However, the energy as independent variable is continuously provided by the *in situ* high pressure which replaces hv with hx. The energy of hx increases with increasing pressure. As shown in Fig. S1 [44], the Fermi resonance reaches the strongest at 20 GPa, and the energy becomes $2h(v + x) = h(v - x)'$ between the P_1 and P_3 modes. Fermi resonance can occur only when two different vibration modes exhibit the same symmetry (in this case Ag) and nearly equivalent energies, thus leading to the coupling of two modes. When two modes are close to each other caused by energy changes (in this case high pressure), the intensity and characteristics of two modes will transfer to each other. We note that the modes do not cross, and the maximum resonance can be identified when two modes are at the closest positions in the frequency space with the equivalent intensity. Therefore, the maximum Fermi resonance of CTO under high pressure is near 20 GPa, similar to FTO under high pressure (in that case between 18 and 20 GPa) [40].

When undergoing Fermi resonance, the interactions between two modes under high pressure can be described as [45]

$$(v_+ - v_-)^2 = (v_a - v_b)^2 + 4\delta^2, \qquad (8)$$

where v_+ and v_- represent the observed modes; v_a and v_b, the unperturbed mode frequencies; and δ, the coupling constant. Using the relationship $v_+ + v_- = v_a + v_b$, we can calculate the frequencies of the mode that are unperturbed by Fermi resonance under pressure. When CTO is at the maximum Fermi resonance under the pressure near 20 GPa, $v_a = v_b$, $v_+ \approx 218\,\mathrm{cm}^{-1}$, and $v_- \approx 117\,\mathrm{cm}^{-1}$ are obtained. Then the coupling constant δ can be calculated as 45 cm^{-1}, consistent with previous work [40]. Consequently, the observed Raman evidence indicates that the phase in 40 GPa is fully crystalline, because of the existence of two low-frequency modes (199.5 and 255 cm^{-1}) and one higher-frequency mode (799.5 cm^{-1}) as well as the three peaks which are also sharp enough. Furthermore, the Raman spectra have maintained the profile of ilmenite structure until 40 GPa. This is a peculiar phenomenon since few mineral crystals remain stable at 40 GPa. Based on the general line shapes of vibrational modes and the distortion of the TiO_6 octahedron, we predict that a phase transition may occur above 40 GPa.

FIG. 4. (a) Raman spectra of IL-type CoTiO$_3$ at different pressures in the frequency range of 565–855 cm^{-1}. The green dotted lines are a guide to the eye. (b) Pressure dependence of the Raman shift and the full width at half maximum, respectively. (c) Pressure dependence of the peak intensity in four stages at 699.4 cm^{-1} and the schematic of localized surface plasmon resonance (LSPR), order-disorder, respectively. The color indicates signal intensities; maximal intensities are marked by darker shades.

Under extreme conditions, it is very important to establish the thermodynamic equation $PV = nRT$, as well as accurately measuring the parameter of pressure P in the equation. As shown in Fig. 4(a), we have explored the structural stability of CTO under high pressure in detail. The peak around 699.4 cm^{-1} has a more sensitive pressure-induced Raman shift and also keeps a high intensity until 40 GPa, manifesting a strong polarization between Ti and O ions. In addition, the pressure has little effect on its degree of polarization, suggesting an ideal Raman peak suitable for the pressure gauge. To judge the feasibility of the CTO pressure gauge, we focus on investigating the pressure dependence of the Raman shift, FWHM, and peak intensity regarding the 699.4 cm^{-1} mode (Ag). As shown in Fig. 4(b), in order to obtain the first pressure derivatives of the Ag mode (699.4 cm^{-1}), we have fitted the pressure-dependent Raman data by the following equations:

$$\tau(P) = 712.08(1.66)2.25(0.17)P(0 < P < 40\,\text{GPa}), \quad (9)$$

and

$$\Omega(P) = 35.11(0.58) + 0.02(0.01)P(5 < P < 40\,\text{GPa}). \quad (10)$$

Notably, the FWHM dramatically decreases by 35 cm^{-1} from 0.1 to 5 GPa, whereas no further changes are observed between 5 and 40 GPa, indicating a significant increase in the

sample crystallinity accompanied by increasing pressure up to 5 GPa. We assume that the sample transforms from gel (PTM injection into the sample surface gap) to solid (PTM curing) state under pressure. Intriguingly, from Fig. 4(c) we can see that the pressure dependence of the mode intensity does not demonstrate the expected linear relationship. Specifically, the intensity of the 699.4 cm^{-1} mode (Ag) first shows a gradual enhancement within 17 GPa, and then decreases as the pressure is slowly loaded to 40 GPa. To explain the evolution of the mode intensity, possible spatial arrangements of CTO NOVs are proposed [see the insets in Fig. 4(c)]. Because of the unique characteristic of its numerous outer d valence electrons, CTO can exhibit the SPR property with field enhancements [39,46–49].

In order to quantitatively demonstrate the evolution of Raman signals, the effect of plasmon-resonance field enhancement has been introduced and elucidated systematically (Fig. 5). Electromagnetic simulations are performed by a finite element method (FEM) software package, COMSOL MULTIPHYSICS. The dielectric function of CTO is performed by a first-principal calculation and then used in the simulation. Since the SEM and TEM images display the shape of a NOV particle of CTO [see Figs. 1(b) and 1(c)], the sample profile is replaced by NOVs for simulations under compression. In addition, the gap reduction and nanoparticle dislocation dominate the typical features during the pressure loading [36,50–53]. Moreover, the calculated dielectric functions of CTO exhibit the insensitivity to pressure (see Fig. S2 in the
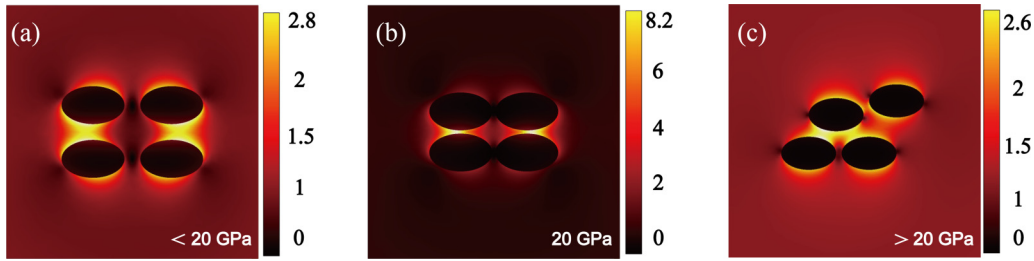
FIG. 5. The simulation of pressure-induced particle distribution: (a) large gaps of nanoparticles, (b) narrow gaps of nanoparticles, and (c) disordered distribution of nanoparticles, respectively. The color bar means the relative intensity of "hot spots."

Supplemental Material [44]). Hence, the simulation under pressure just focuses on the possible spatial arrangement of nanoparticles, and does not involve the minor changes in their physicochemical properties.

As the average nanoparticle gap of adjacent CTO NOVs is about 100 nm at ambient conditions [see Fig. 1(b)], the PTM (methanol : ethanol : water = 16 : 3 : 1) is injected into the cavity where the nanoparticles are located. It is easy to soak the sample surface from a solid to a gel state. Since the crystallinity of the gel is lower than that of the solid state, the FWHM of the Raman mode will be broadened and the peak intensity will be weakened at lower pressure [see stage I in Fig. 4(c)]. The intensity of the 699.4 cm^{-1} mode becomes stronger in stages I and II, because of the electric-field enhancement arising from the pressure-induced reduction of nanoparticle gaps in the range of 10–100 nm [see Figs. 5(a) and 5(b) for the schematic illustration]. Under such configurations, we have computed the scattering spectra as shown in Fig. S3 [44] and observed a weak resonant mode around 532 nm from the structure in Fig. S4(b), whereas other two structures from Figs. S4(a) and S4(c) [44] are off resonance (data omitted). Regarding the corresponding field profiles, we can observe that the maximum local-field enhancement in Fig. 5(b) can reach to 8.2 whereas the intensity in Fig. 5(c) is only 2.8. Such a high local-field enhancement may serve as the increase of the 699.4 cm^{-1} peak at stages I and II.

When the pressure in the DAC chamber continues to increase, the interparticle dislocation occurs (Fig. S4(c) [44]). As a result, the corresponding local-field enhancement decreases to 2.6 [Fig. 5(c)], resulting in a decrease in peak intensity at stage III in Fig. 4(c). In terms of the molecular scale, the local CoO_6 octahedron in the CTO crystal lattice begins to distort at 17 GPa [see Fig. 2(b)], indicating that the Co and O atoms begin to undergo "order-disorder" transformation. Consequently, the intensity of the 699.4 cm^{-1} mode turns to decrease at stage III due to two negative factors including simultaneous particle dislocation and atomic disorder. Notably, when the interparticle gap is reduced to the subnanometer scale (<1 nm), the quantum effect such as electron tunneling becomes important (from Figs. S4(d) and S4(e) [44]). Since the tunneling current between nanoparticles causes short circuits in the junction, the Coulomb coupling between the charges of opposite sign in two nanoparticles will decrease, and it strongly reduces the local electromagnetic field enhancement [54]. Consequently, the Raman intensity continues to decrease at stages III and IV [see Fig. 4(c)]. Furthermore, owing to the enhancement of the nonhydrostatic condition after 30 GPa, the intensity of the 699.4 cm^{-1}

mode at stage IV decreases more rapidly than at stage III. The nonhydrostatic pressure can accelerate the "order-disorder" transition of Co and O ions in the lattice and increase tunneling-electron current.

In addition, two traditional pressure gauges (quartz and ruby) were also performed by *in situ* high-pressure Raman experiments for a comparison [25,55,56]. For the sake of simplicity, the calibration peak of quartz corresponding to the Si-O vibration mode (465 cm^{-1}, Ag) is mainly discussed. As shown in Fig. S5(a) [44], the relaxation of the calibration peak at 19–26 GPa and the amorphization of quartz above 28 GPa determine that quartz is only suitable for low-pressure measurements, in agreement with previous studies [57,58]. Besides, the Raman spectra of ruby at different pressures in the frequency range 4000–5500 cm^{-1} were performed (Fig. S5(b) [44]). As the pressure increases, the ruby R_1 line (4400 cm^{-1}) easily shifts to 4800 cm^{-1} at 63.5 GPa, which can be calculated by the following empirical equation :

$$P\text{GPa} = \frac{a}{b}\left\{\left(\frac{\lambda_0 + \Delta\lambda}{\lambda_0}\right)^b - 1\right\}. \qquad (11)$$

Here, parameters are set as $a = 19.04$, $b = 5$, and $\lambda_0 = 694.2$ Å. $\Delta\lambda = \lambda_p - \lambda_0$ represents the blueshift value of the R_1 line under pressure and λ_p is the frequency of the Raman mode under P pressure. Although ruby is an excellent pressure gauge, CTO can be considered as a pressure gauge for some pressure-induced fluorescence emission materials with high frequency, such as Cs_4PbBr_6, $CH_3NH_3PbBr_3$, and others [59,60]. Therefore, it is necessary to find a pressure gauge that meets both low-frequency and ultrahigh-pressure conditions.

Calcite, dolomite, magnesite, and other minerals have been proposed for Raman spectral pressure gauges in addition to ruby and quartz, each of which has its own advantages [25,26]. Herein, the parameters of three pressure gauges in this study are summarized in Table II when the PTM is methanol : ethanol : water = 16 : 3 : 1. Naturally, choos-

TABLE II. The parameters of three scales for pressure when PTM is methanol : ethanol : water = 16 : 3 : 1.

	Pressure (GPa)	Range (cm^{-1})	FWHM (cm^{-1})	Intensity	Slope
IL-type CTO	40$^+$	699.5–799$^+$	35	Medium	Weak
Quartz	20	469–580	8.5–15	Weak	Medium
Ruby	63.5$^+$	4400–4800$^+$	33–150$^+$	Strong	Strong

ing suitable pressure gauges by experimental conditions will benefit the reliability of the observed results.

IV. CONCLUSIONS

In summary, we have fabricated the ilmenite $CoTiO_3$ nano-ovals by the sol-gel method and quantitatively investigated its vibrational properties and pressure-gauge behaviors by *in situ* high-pressure Raman experiments. The ilmenite $CoTiO_3$ exhibits excellent lattice stability without phase transition and amorphization up to 40 GPa. This result has been well elucidated by the Jahn-Teller effect and Fermi resonance as well as the mode Grüneisen parameters. Additionally, we have also demonstrated that the evolution of Raman signals for a pressure gauge can be satisfactorily explained by the plasmon-enhanced effect. Our study suggests a good pressure gauge for high-pressure measurement in the low-frequency range, and offers insights for exploring the Raman behavior of other ilmenite-based functional materials under extreme conditions.

[1] P. E. Janolin, P. Bouvier, J. Kreisel, P. A. Thomas, I. A. Kornev, L. Bellaiche, W. Crichton, M. Hanfland, and B. Dkhil, Phys. Rev. Lett. **101**, 237601 (2008).

[2] Y. Cui, G. Zhang, H. Li, H. Lin, X. Zhu, H.-H. Wen, G. Wang, J. Sun, M. Ma, Y. Li, D. Gong, T. Xie, Y. Gu, S. Li, H. Luo, P. Yu, and W. Yu, Sci. Bull. **63**, 11 (2018).

[3] K. R. O'Neal, A. J. Clune, N. C. Harms, S.-W. Cheong, J. Yang, Z. Liu, T. Birol, and J. L. Musfeldt, Phys. Rev. B **98**, 184101 (2018).

[4] H. Sun, M. Yao, Y. Song, L. Zhu, J. Dong, R. Liu, P. Li, B. Zhao, and B. Liu, Nanoscale **11**, 21493 (2019).

[5] P. Li, X. Wang, H. Li, X. Yang, X. Zhang, L. Zhang, Y. Ozaki, B. Liu, and B. Zhao, Chem. Commun. **54**, 6280 (2018).

[6] F. D. Cortes Vega, P. G. Martinez Torres, J. Pichardo Molina, N. M. Gomez Ortiz, V. G. Hadjiev, J. Zarate Medina, and F. C. Robles Hernandez, J. Mater. Chem. C **5**, 4959 (2017).

[7] J. Lin, J. Yu, O. U. Akakuru, X. Wang, B. Yuan, T. Chen, L. Guo, and A. Wu, Chem. Sci. **11**, 9414 (2020).

[8] Z. Luo, H. Liu, W. Shen, K. Shi, A. Chen, L. Sheng, Y. Sui, and B. Zou, Chem. Res. Chin. Univ. **38**, 843 (2022).

[9] Q. Zhu, S. Jiang, K. Ye, W. Hu, J. Zhang, X. Niu, Y. Lin, S. Chen, L. Song, Q. Zhang, J. Jiang, and Y. Luo, Adv. Mater. **32**, 2004059 (2020).

[10] L. Li and J. Y. Li, Phys. Rev. B **73**, 184416 (2006).

[11] A. M. Shuvaev, V. D. Travkin, V. Y. Ivanov, A. A. Mukhin, and A. Pimenov, Phys. Rev. Lett. **104**, 097202 (2010).

[12] T. M. Pan, T. F. Lei, and T. S. Chao, J. Appl. Phys. **89**, 3447 (2001).

[13] J. Zou and W. Zheng, Ceram. Int. **42**, 8198 (2016).

[14] J. Lu, Y. Jiang, Y. Zhang, J. Huang, and Z. Xu, Ceram. Int. **41**, 3714 (2015).

[15] A. V. Agafonov and A. V. Vinogradov, High Energy Chem. **42**, 578 (2008).

[16] R. Tursun, Y. C. Su, Q. S. Yu, J. Tan, T. Hu, Z. B. Luo, and J. Zhang, J. Alloys Compd. **773**, 288 (2019).

[17] W. Qi and A. Hushur, Eur. Phys. J. B **95**, 30 (2022).

[18] T. Bernert, J. Ruiz-Fuertes, L. Bayarjargal, and B. Winkler, Solid State Sci. **43**, 53 (2015).

[19] S. Guo, K. Bu, J. Li, Q. Hu, H. Luo, Y. He, Y. Wu, D. Zhang, Y. Zhao, W. Yang, M. G. Kanatzidis, and X. Lu, J. Am. Chem. Soc. **143**, 2545 (2021).

[20] L. Dubrovinsky, S. Khandarkhaeva, T. Fedotenko, D. Laniel, M. Bykov, C. Giacobbe, E. L. Bright, P. Sedmak, S. Chariton, V. Prakapenka, A. V. Ponomareva, E. A. Smirnova, M. P. Belov, F. Tasnádi, N. Shulumba, F. Trybel, I. A. Abrikosov, and N. Dubrovinskaia, Nature (London) **605**, 274 (2022).

[21] W. Sun, L. Dai, H. Hu, M. Wang, Z. Hu, and C. Jing, Front. Earth Sci. **10**, 861003 (2022).

[22] X. Wu, S. Qin, and L. Dubrovinsky, Geosci. Front. **2**, 107 (2011).

[23] N. Zhang, N. Dygert, Y. Liang, and E. M. Parmentier, Geophys. Res. Lett. **44**, 6543 (2017).

[24] M. N. Iliev and M. V. Abrashev, J. Raman Spectrosc. **32**, 805 (2001).

[25] J. H. Eggert, K. A. Goettel, and I. F. Silvera, Phys. Rev. B **40**, 5724 (1989).

[26] Q. Y. Hu, J. F. Shu, W. G. Yang, C. Park, M. W. Chen, T. Fujita, H. K. Mao, and H. W. Sheng, Phys. Rev. B **95**, 104112 (2017).

[27] X. Yuan, X. Xiong, G. Zhang, and R. A. Mayanovic, J. Raman Spectrosc. **51**, 1248 (2020).

[28] I. Kocas and M. Bergoglio, Measurement **45**, 2486 (2012).

[29] B. Schuster, C. Weikusat, R. Miletich, C. Trautmann, R. Neumann, and F. Fujara, Phys. Rev. B **82**, 184110 (2010).

[30] S. Bai and K. Sugioka, Light Sci. Appl. **2**, 13 (2021).

[31] J. Langer, D. Jimenez de Aberasturi, J. Aizpurua, R. A. Alvarez-Puebla, B. Auguie, J. J. Baumberg, G. C. Bazan, S. E. J. Bell, A. Boisen, A. G. Brolo, J. Choo, D. Cialla-May, V. Deckert, L. Fabris, K. Faulds, F. J. Garcia de Abajo, R. Goodacre, D. Graham, A. J. Haes, C. L. Haynes *et al.*, ACS Nano **14**, 28 (2020).

[32] S. E. Heo and J. W. Ha, Biochip. J. **16**, 183 (2022).

[33] X. Liu and M. T. Swihart, Chem. Soc. Rev. **43**, 3908 (2014).

[34] B. X. Yan, Y. Y. Zhu, Y. Wei, and H. Pei, Sci. Rep. **11**, 8391 (2021).

[35] G. Barbillon, Photonics **7**, 53 (2020).

[36] M. A. Schroer, F. Lehmkühler, V. Markmann, L. Frenzel, J. Möller, H. Lange, G. Grübel, and F. Schulz, J. Phys. Chem. C **123**, 29994 (2019).

[37] J. Chen, H. Cheng, X. Zhou, X. Yan, L. Wang, Y. Zhao, and S. Wang, Rev. Sci. Instrum. **92**, 033905 (2021).

[38] M. Martínez-Reina, E. Amado-González, and W. Goméz-Jaramillo, J. Solution Chem. **44**, 206 (2015).

[39] R. M. Dubrovin, N. V. Siverin, M. A. Prosnikov, V. A. Chernyshev, N. N. Novikova, P. C. M. Christianen, A. M. Balbashov, and R. V. Pisarev, J. Alloys Compd. **858**, 157633 (2021).

[40] C. E. Vennari and Q. Williams, Phys. Chem. Miner. **48**, 34 (2021).

[41] R. Vilarinho, D. J. Passos, E. C. Queirós, P. B. Tavares, A. Almeida, M. C. Weber, M. Guennou, J. Kreisel, and J. A. Moreira, Phys. Rev. B **97**, 144110 (2018).

[42] B. J. Kennedy, J. Ting, Q. Zhou, Z. Zhang, M. Matsuda, and M. Miyake, J. Solid State Chem. **182**, 954 (2009).

[43] T. R. Cunha, A. D. Rodrigues, J. E. Rodrigues, D. V. Sampaio, B. J. A. Moulton, R. C. da Costa, and P. S. Pizani, Solid State Sci. **88**, 1 (2019).

[44] See Supplemental Material at http://link.aps.org/supplemental/10.1103/PhysRevB.107.085429 for the pressure-dependence Fermi resonance of CoTiO$_3$, the pressure-dependence dielectric functions of CiTiO$_3$, the scattering spectrum of CoTiO$_3$ under visible light, the schematics of pressure-induced particle distribution, and Raman spectra of quartz and ruby at different pressures.

[45] H. Shimizu, Phys. Rev. B **32**, 4120 (1985).

[46] T. Acharya and R. N. P. Choudhary, Phys. B (Amsterdam) **582**, 411970 (2020).

[47] J. Li, X. Xu, B. Huang, Z. Lou, and B. Li, ACS Appl. Mater. Inter. **13**, 10047 (2021).

[48] K. Manthiram and A. P. Alivisatos, J. Am. Chem. Soc. **134**, 3995 (2012).

[49] C. Zhu and Q. Xu, Chem. Asian J. **13**, 730 (2018).

[50] C. Pantea, J. Gubicza, T. Ungár, G. A. Voronin, N. H. Nam, and T. W. Zerda, Diamond Relat. Mater. **13**, 1753 (2004).

[51] B. Chen, H. Zhang, K. A. Dunphy-Guzman, D. Spagnoli, M. B. Kruger, D. V. S. Muthu, M. Kunz, S. Fakra, J. Z. Hu, Q. Z. Guo, and J. F. Banfield, Phys. Rev. B **79**, 125406 (2009).

[52] Z. Gao, Z. Xiong, J. Li, C. Lu, G. Zhang, T. Zeng, Y. Ma, G. Ma, R. Zhang, K. Chen, T. Zhang, Y. Liu, J. Yang, L. Cao, and K. Jin, J. Mater. Chem. A **7**, 3384 (2019).

[53] J. Amodeo, S. Merkel, C. Tromas, P. Carrez, S. Korte-Kerzel, P. Cordier, and J. Chevalier, Crystals **8**, 240 (2018).

[54] R. Esteban, A. G. Borisov, P. Nordlander, and J. Aizpurua, Nat. Commun. **3**, 825 (2012).

[55] M. V. Hopson and S. K. Treadway, Int. J. Impact Eng. **35**, 1593 (2008).

[56] N. Matsumoto, Y. Sudo, B. K. Sinha, and M. Niwa, IEEE Trans. Ultrason., Ferroelectr. Freq. Control **47**, 346 (2000).

[57] J. K. Kathleen, M. Charles, J. H. Russell, H. K. Mao, and R. V. David, Science **259**, 666 (1993).

[58] R. J. Hemley, A. P. Jephcoat, H. K. Mao, L. C. Ming, and M. H. Manghnani, Nature (London) **334**, 52 (1988).

[59] Z. Ma, Z. Liu, S. Lu, L. Wang, X. Feng, D. Yang, K. Wang, G. Xiao, L. Zhang, S. A. T. Redfern, and B. Zou, Nat. Commun. **9**, 4506 (2018).

[60] T. Yin, Y. Fang, W. K. Chong, K. T. Ming, S. Jiang, X. Li, J. L. Kuo, J. Fang, T. C. Sum, T. J. White, J. Yan, and Z. X. Shen, Adv. Mater. **30**, 1705017 (2018).